Journal of Catalysis 278 (2011) 16–25

Contents lists available at ScienceDirect

Journal of Catalysis

journal homepage: www.elsevier.com/locate/jcat

Methane oxidation on Pd–Ceria: A DFT study of the mechanism over $Pd_xCe_{1-x}O_2$, Pd, and PdO

Adam D. Mayernick, Michael J. Janik *

Department of Chemical Engineering, Pennsylvania State University, University Park, PA 16802, United States

ARTICLE INFO

Article history:
Received 9 August 2010
Revised 29 October 2010
Accepted 11 November 2010
Available online 24 December 2010

Keywords:
Ceria
DFT + *U*
Palladium
Methane
Oxidation
Supported catalysis

ABSTRACT

Palladium/ceria exhibits unique catalytic activity for hydrocarbon oxidation; however, the chemical and structural properties of active sites on the palladium–ceria surface are difficult to characterize. Strong interactions between palladium and the ceria support stabilize oxidized $Pd^{\delta+}$ species, which may contribute to the significant activity of Pd/ceria for methane oxidation. We present a density functional theory (DFT + *U*) investigation into methane oxidation over Pd/ceria and quantify the activity of the $Pd_xCe_{1-x}O_2$(1 1 1) mixed oxide surface in comparison with the PdO(1 0 0) and Pd(1 1 1) surfaces. The methane activation barrier is lowest over the $Pd_xCe_{1-x}O_2$(1 1 1) surface, even lower than over the Pd(1 1 1) surface or low coordinated stepped or kinked Pd sites. Subsequent reaction steps in complete oxidation, including product desorption and vacancy refilling, are considered to substantiate that methane activation remains the rate-limiting step despite the low barrier over $Pd_xCe_{1-x}O_2$(1 1 1). The low barrier over the $Pd_xCe_{1-x}O_2$(1 1 1) surface demonstrates that mixed ceria-noble metal oxides offer the potential for improved hydrocarbon oxidation performance with respect to dispersed noble metal particles on ceria.

1. Introduction

Ceria offers unique properties as a heterogeneous catalyst support or active component, of which the redox properties [1–4] and methane oxidation activity [5,6] can be altered by the addition of low levels of noble metals such as palladium. The oxidation state and morphology of Pd species on Pd/ceria are a function of preparation method [5,7–12] and catalytic operating conditions [7,12–14]. Palladium can be supported on ceria as metal particles [12,15] or PdO_x species [8,11,16], and strong interactions between Pd and the ceria support may stabilize a surface mixed oxide phase ($Pd_xCe_{1-x}O_y$) [5,13,17]. Each of the chemically distinct Pd species on Pd/ceria likely provides unique catalytic activity; however, which sites contribute to the significant activity for methane oxidation are unclear. Computational methods have been used to probe the relative stability of Pd species on ceria [5,13] and to evaluate elementary reaction energies for methane oxidation over pure CeO_2 [18]; however, the catalytic activity of ceria-supported Pd species has not been investigated. We present a computational investigation, utilizing density functional theory, into methane complete oxidation over the CeO_2(1 1 1), $Pd_xCe_{1-x}O_2$(1 1 1), and PdO(1 0 0) surfaces, in comparison with C–H activation on Pd metal surfaces. The reaction barrier for methane oxidation is lowest over the $Pd_xCe_{1-x}O_2$(1 1 1) surface, suggesting that this Pd/ceria surface mixed oxide provides unusually high catalytic activity. Our results detail the rate-determining steps and stable intermediates for methane oxidation over each surface.

The oxidation state of palladium and the morphology of the palladium surface are strongly a function of catalytic operating conditions, which complicates characterization efforts to elucidate the nature of the active site for methane oxidation. *Ex situ* characterization can be used to determine the Pd oxidation state before and after reaction; however, these efforts illustrate further the complexity in determining the structure and functionality of the active phase. Hoflund et al. report ELS and XPS spectroscopy results which show that PdO forms during methane combustion on palladium powder [19]. The bulk transition for PdO decomposition to Pd occurs at approximately 1070 K in 1 atm O_2 [20]; however, oxidation of small Pd particles may occur at lower temperatures. Ribeiro et al. show that PdO decomposes to Pd at 907 K in 1.5 torr O_2, and that this transition results in an order of magnitude drop in the methane combustion turnover rate [21]. Thus, depending upon the temperature and oxygen pressure, Pd or PdO species may be stable, with dramatic effects on catalytic activity. For Pd on ceria, the dependence of the stable surface structure and oxidation state on reaction conditions is even more complex, as Pd, PdO, or $Pd_xCe_{1-x}O_y$ may be stable during reaction.

The morphology and oxidation state of Pd on ceria are both strong functions of synthesis and pretreatment methods, and strong interactions between Pd and ceria stabilize oxidized Pd

* Corresponding author. Address: 104 Fenske Laboratory, University Park, PA 16802, United States. Fax: +1 814 865 7846.
E-mail address: mjanik@psu.edu (M.J. Janik).

0021-9517/$ - see front matter © 2010 Elsevier Inc. All rights reserved.
doi:10.1016/j.jcat.2010.11.006

species. X-ray photoelectron spectroscopy (XPS) showed that Pd/ceria prepared by deposition–precipitation had a higher concentration of cationic $Pd^{\delta+}$ sites than Pd/ceria prepared by wet impregnation [8]. Preparation of Pd/ceria by solution-combustion synthesis methods can facilitate mixing of Pd atoms into the CeO_2 lattice framework [5,17]. A combination of XPS, X-ray diffraction (XRD), and extended X-ray absorption fine structure (EXAFS) results was used to determine that Pd/ceria prepared by solution-combustion synthesis contains Pd^{2+} cations incorporated into cubic fluorite CeO_2 as a solid solution, whereas wet impregnation results in samples containing primarily metallic Pd [17]. Colussi et al. also recently reported that surface solid solutions of Pd^{2+}/CeO_x with distinct short and long range order can be prepared by solution-combustion synthesis [5]. High-resolution transmission electron microscopy (HRTEM) and DFT calculations confirm that their Pd^{2+}/CeO_x samples consist of a reconstructed CeO_2(1 1 0) surface with Pd^{2+} ions substituted for Ce^{4+} [5].

Palladium is an active catalyst for methane oxidation [19,21], and the interaction between Pd and a ceria support facilitates unique oxidation activity [5]. The oxidation rate on Pd/ceria exceeds the rate over pure ceria, with particularly high catalytic activity displayed by Pd/ceria catalysts containing oxidized $Pd^{\delta+}$ species or Pd–O–Ce linkages. For the direct oxidation of methane in a solid oxide fuel cell (SOFC), the addition of 1 wt.% Pd to a pure ceria anode increased the maximum power density by a factor of 10 [6]. The rate of methane combustion on Pd^{2+}/CeO_x mixed surface oxides of 1 and 1.71 wt.% Pd was nearly twice that of Pd/ceria samples of equivalent composition prepared by incipient wetness [5]. Despite numerous studies illustrating the catalytic activity of Pd/ceria for methane oxidation, characterization of active sites is challenged by the heterogeneity of the metal/metal oxide structure and structural changes which may occur during reaction. The computational chemistry methods utilized herein probe the catalytic activity of CeO_2, $Pd_xCe_{1-x}O_2$, PdO, and Pd to isolate the contributions of each to the overall oxidation performance of Pd/ceria catalysts.

Computational chemistry methods can directly evaluate the relative energies of elementary reaction steps and activation barriers on heterogeneous supported catalysts; however, applying these methods to study catalytic reactions on ceria has been limited to the consideration of simple redox reaction mechanisms. Previous computational studies of hydrocarbon chemistry on ceria have focused on evaluating elementary reaction energies for CO oxidation [18,22,23] and H_2/H_2O cycling [24,25] on pure CeO_2, as well as CO oxidation on CeO_2 doped with single transition metal atoms such as Au, Ag, Cu [26], and Zr [27]. The structural changes that result from doping as well as the effects of doping on reducibility have also been investigated using DFT methods for noble metal atoms such as Pd [28] and Pt [29]. Knapp et al. evaluated the reaction energy diagram for methane combustion to CO_2 over pure CeO_2(1 1 1) [18], though the reaction energetics in the presence of added transition or noble metals was not considered. Herein, we report the reaction energetics for the oxidation of CH_4 to CO_2 over Pd/ceria to establish a complete methane oxidation cycle and quantify changes in catalytic activity upon formation of $Pd_xCe_{1-x}O_2$. We compare the reaction energetics over CeO_2(1 1 1) and $Pd_xCe_{1-x}O_2$(1 1 1) to those over PdO(1 0 0) and Pd to distinguish the catalytic activity of the Pd/ceria mixed oxide from that of other Pd species.

Our previous study used *ab initio* thermodynamics to evaluate the stability of different Pd species on CeO_2(1 1 1), (1 1 0), and (1 0 0) surfaces. Under varying operating conditions, the $Pd_xCe_{1-x}O_2$(1 1 1) surface is stable with respect to other single atom states of Pd on the CeO_2(1 1 1) surface [13]. The oxygen vacancy formation energy on $Pd_xCe_{1-x}O_2$(1 1 1) is less endothermic than on CeO_2(1 1 1), and the methane activation barrier is lower over $Pd_xCe_{1-x}O_2$(1 1 1) than over CeO_2(1 1 1). This work utilizes density functional theory to calculate the reaction free energies of elementary steps in methane oxidation over CeO_2(1 1 1), $Pd_xCe_{1-x}O_2$(1 1 1), and PdO(1 0 0) in comparison with C–H activation on Pd metal sites. These models represent the surface facets of a pure ceria (CeO_2(1 1 1)), palladium/ceria mixed oxide ($Pd_xCe_{1-x}O_2$(1 1 1)), or palladium oxide (PdO(1 0 0)) particle, respectively. Evaluation of the oxidation mechanism over each of these surfaces facilitates comparison between the catalytic activity of Pd/ceria mixed oxides, PdO, and Pd metal. Regardless of the initial oxidation state, the oxidation state of Pd cycles between either Pd^0/Pd^{2+} or Pd^{2+}/Pd^{4+} during the full reaction turnover of methane oxidation. We report the activation barriers, rate-determining steps, and stable intermediates for methane oxidation over each surface, with discussion of adsorption sites and adsorbate geometries. We use *ab initio* thermodynamics to evaluate the dependence of rate-determining steps and the overall reaction mechanism on catalytic operating conditions including temperature and partial pressure of reactants and products. We specifically consider operating regimes corresponding to catalytic combustion experiments and SOFC operation.

2. Methods

2.1. Electronic structure method

Calculations were made using the Vienna *ab initio* simulation program (VASP), an *ab initio* total-energy and molecular dynamics program developed at the Institute for Material Physics at the University of Vienna [30–32]. The projector augmented wave method [33] was used to represent the core region, with valence electron wavefunctions expanded in a tractable plane wave basis set. The energy cutoffs of the plane wave basis sets used herein were 400 eV, 450 eV, and 500 eV for Pd metal, CeO_2, and PdO, respectively (chosen to ensure convergence of total energy with respect to energy cutoff). Valence configurations were $5s^2 5p^6 6s^2 4f^1 5d^1$ for cerium, $2s^2 2p^4$ for oxygen, $4d^{10}$ for Pd, $2s^2 2p^2$ for C, and $1s^1$ for H. Structural optimizations were performed by minimizing the forces on all atoms to below 0.05 eV $Å^{-1}$, and all calculations for CeO_2 and PdO were spin-polarized. The Perdew–Wang (PW91) version of the generalized gradient approximation (GGA) was used to incorporate exchange and correlation energies [34].

Due to well-established difficulties within DFT to accurately represent the nature of 4*f* states in ceria [35–37], we implemented the DFT + *U* approach. The DFT + *U* method introduces the Hubbard *U* term as an on-site Coulombic interaction in the *f* states of ceria, which properly localizes electrons in these states for reduced ceria structures (CeO_{2-x}, or more generally $Ce_x^{3+}Ce_{1-x}^{4+}O_y$). We do not directly consider ceria surfaces reduced by oxygen vacancies herein; however, our previous study illustrated that the adsorption of H atoms and CH_3 groups on pure CeO_2 reduces surface Ce^{4+} cations to Ce^{3+} [38]. We used a value of $U = 5$ eV, which is consistent with recommended values within the DFT + *U* method used in previous studies of ceria [18,28,39–42]. Our previous study included evaluation of the dependence of methane activation and oxygen vacancy formation on the value of the Hubbard *U* term on CeO_2 and $Pd_xCe_{1-x}O_2$. For pure CeO_2, the vacancy formation energy and methane adsorption energy increase in exothermicity linearly with increasing *U* value (ΔE_{vac} and ΔE_{ads} are proportional to $0.4\Delta U$ (eV)) [38]. Given the dependence of vacancy formation energy and adsorption energy on the U value for pure ceria, the quantitative values we calculate are inherently dependent on our specific choice of *U* value. For $Pd_xCe_{1-x}O_2$, the vacancy formation energy and methane adsorption energy become less exothermic with increasing *U* value, however, with much less dependence on *U*

value than for pure ceria as Pd^{4+} is reduced rather than Ce^{4+} (ΔE_{vac} and ΔE_{ads} are proportional to $-0.05\Delta U$ (eV)) [38]. We use a U value of 5 eV to accurately describe the electronic structure of reduced ceria, and the qualitative comparisons of reaction energies we report over $Pd_xCe_{1-x}O_2$ and Pd or PdO are not sensitive to the Ce 4f U value.

2.2. Surface models

Fig. 1 displays the slab models used for the CeO_2(1 1 1), $Pd_xCe_{1-x}O_2$ (1 1 1), and PdO(1 0 0). The mirrored slab model includes symmetrical adsorbates on both sides of the slab. The ceria surface is modeled as a 12-layer ($Ce_{16}O_{32}$) mirrored slab of the (1 1 1) termination of cubic fluorite CeO_2 separated by 15 Å of vacuum in the direction perpendicular to the surface. The surface energy of CeO_2(1 1 1) is lowest among single crystal terminations of ceria [38–40], indicating that this surface termination will represent a large portion of a polycrystalline CeO_2 surface. The mirrored slab model of the ceria surface was used specifically to minimize slab-to-slab interactions that may result from a large net surface dipole moment upon the interaction of the surface with adsorbates and the reduction in surface metal ions. The Brillouin zone was sampled using a $(2 \times 2 \times 1)$ MP grid for the (1 1 1) surface, with the third vector perpendicular to the surface. We use a $p(2 \times 2)$ expansion of the surface unit cell, which results in a termination of four surface oxygen atoms on each side of the slab and four Ce atoms in the atomic layer below.

The PdO(1 0 0) surface was modeled as a slab of tetragonal palladium (II) oxide (PdO), respectively, also separated by 15 Å of vacuum in the direction perpendicular to the surface. The lattice parameters of bulk PdO were optimized within 2% of the corresponding experimentally determined value [43,44]. We used a 9-layer mirrored slab with a (2×1) expansion to model the PdO(1 0 0) surface, with all layers allowed to relax during structural optimizations. Scheffler et al. used DFT and *ab initio* thermodynamics to show that the surface formation energy of the (1 0 0) termination of PdO is less endergonic than all other single crystal terminations of PdO at O_2 pressures above 10^{-30} atm at 300 K [45], motivating its use in this study.

Methane activation barriers are also reported over Pd(1 1 1) and Pd^*/CeO_2 model systems to provide comparison to the Pd^0 oxidation state. Description of these models is included in the Supplementary material.

2.3. Reaction free energies

Reaction intermediates for methane oxidation over each surface were optimized by placing one adsorbate of the formula $C_1H_xO_y$ (with $0 \leqslant x \leqslant 2$ and $0 \leqslant y \leqslant 2$), or an isolated H atom adsorbate, in each surface unit cell. For each $C_1H_xO_y$ adsorbate, the O in $C_1H_xO_y$ corresponds to oxygen bound to the carbon atom which is not lattice oxygen of the stoichiometric surface. Each adsorbate was placed at all high symmetry adsorption sites and configurations on each surface, and the lowest energy adsorption configuration for each adsorbate–surface pair was used to calculate the relative energies of elementary reaction steps. Using one adsorbate per unit cell results in a relatively low coverage of reaction intermediates. For example, H^* on CeO_2(1 1 1) consists of an H atom adsorbed atop one of the four surface oxygen atoms in the unit cell, corresponding to an effective H coverage of 25%. Therefore, reaction energies and analysis reported herein approximate the low coverage limit for methane oxidation. Harmonic vibrational modes were calculated to determine zero-point vibrational energy (ZPVE) corrections to the total energy of isolated molecules and adsorbed species. Optimizations of isolated gas-phase molecules were performed with one free molecule within a $15 \times 15 \times 15$ Å unit cell. The free energies of gas-phase molecules and surface adsorbates were calculated as the sum of the electronic energy (E_{DFT}), ZPVE correction, entropy (ST), and a pressure volume term (PV) as follows:

$$G_{gas} = E_{DFT} + \mathrm{ZPVE} - (S_{vib} + S_{trans} + S_{rot} + S_{elec})T + \mathrm{PV} \quad (1)$$

For surface adsorbates, translational and rotational entropy terms are zero, and the electronic term is included only for gas-phase oxygen. Constrained vibrational calculations were done for adsorbed species, where the Hessian matrix is populated solely with the second derivatives of energy with respect to position of the adsorbate atoms. Configurational entropies of adsorbed species were neglected as they are less than 0.02 eV in all cases. Free energy differences for elementary reaction steps were calculated by subtracting the sum of free energies of the initial state from the sum of free energies of the product state, as follows for the example of CH_3 dissociation to adsorbed CH_2 and H fragments ($CH_3^* + * \rightarrow CH_2^* + H^*$):

$$\Delta G_{rxn,CH_3^*+*\rightarrow CH_2^*+H^*} = \frac{[G_{CH_2^*} + G_{H^*}] - [G_{CH_3^*} + G_{bare}]}{2} \quad (2)$$

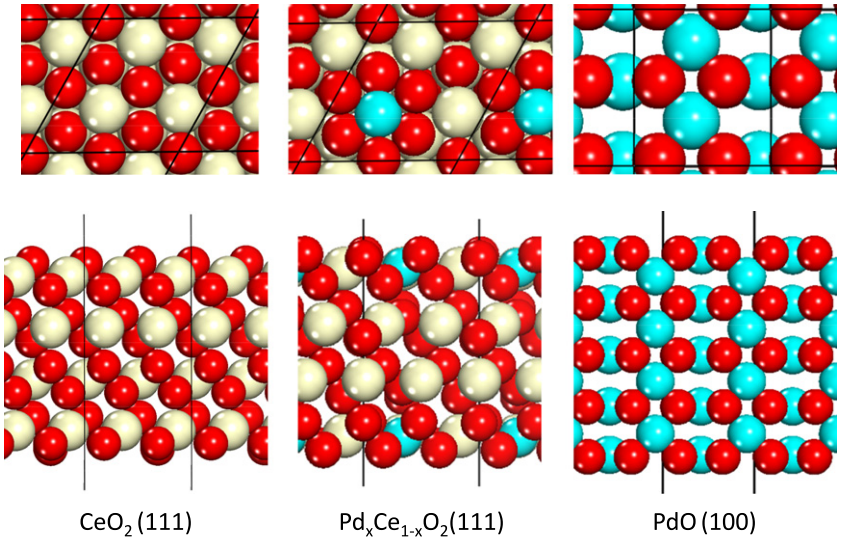

Fig. 1. Top and side views of slab models for CeO_2(1 1 1), $Pd_xCe_{1-x}O_2$(1 1 1), and PdO(1 0 0) surface. Ce is displayed as tan (light), Pd as light blue (gray), and O as red (dark). (For interpretation of the references to colour in this figure legend, the reader is referred to the web version of this article.)

where $G_{CH_2^*}$, G_{H^*}, and $G_{CH_3^*}$ represent the free energies of adsorbed CH_2, H, and CH_3 species, respectively, and G_{bare} is the DFT energy of the bare surface. The denominator of two is included in Eq. (2) for energies calculated over the CeO_2(1 1 1), PdO(1 0 0), Pd*/CeO_2(1 1 1), and $Pd_xCe_{1-x}O_2$(1 1 1) surfaces to account for the fact that mirrored slab models are used with one adsorbate on each side of the mirrored slab. Partial oxidation as well as total combustion pathways involving C–H breaking, O–H forming, and C–O forming steps were considered over the various surface models.

To evaluate the minimum energy path for methane oxidation ($CH_4 + 2O_2 \rightarrow CO_2 + 2H_2O$) over each surface, we also considered the formation energy of CO_2(g) and H_2O(g) from reaction intermediates. Water is formed by adsorption of H atoms on surface oxygen atoms followed by desorption of H_2O(g) to leave a surface oxygen vacancy. The formation energy of H_2O(g) from H* was calculated on the CeO_2(1 1 1), $Pd_xCe_{1-x}O_2$(1 1 1), and PdO(1 0 0) surfaces, as:

$$\Delta G_{H_2O\_formation} = \frac{[2 \cdot G_{H_2O} + G_{vacant} + G_{bare}] - 2 \cdot G_{H^*}}{2} \quad (3)$$

where G_{H^*} is the free energy of adsorbed H (Eq. (1)), G_{H_2O} is the free energy of H_2O(g) (Eq. (1)), and G_{vacant} is the DFT energy of the surface containing an oxygen vacancy on each side of the mirrored slab. Water formation steps are included in the reaction energy diagrams reported herein as elementary steps immediately following C–H breaking steps which result in H* formation. For example, we consider the following three elementary steps for the dissociation of CH_3 to CH_2 $[CH_3^* + \frac{1}{4}O_2(g) \rightarrow CH_2^* + \frac{1}{2}H_2O(g)]$ on the CeO_2(1 1 1), $Pd_xCe_{1-x}O_2$(1 1 1), and PdO(1 0 0) surfaces:

(A) $CH_3^* + * \rightarrow CH_2^* + H^*$

(B) $H^* \rightarrow \frac{1}{2}H_2O(g) + \frac{1}{2}V_{\ddot{O}} + \frac{1}{2}*$

(C) $\frac{1}{2}V_{\ddot{O}} + \frac{1}{4}O_2(g) \rightarrow \frac{1}{2}*$

where $V_{\ddot{O}}$ represents a surface oxygen vacancy.

The consideration of product formation and vacancy filling sequentially throughout the mechanism can be contrasted with the approach of Knapp et al. [18]. Knapp et al. included all water formation energies at the final step and neglected vacancy filling in their analysis of the reaction energy diagram for methane oxidation over pure CeO_2(1 1 1). The authors report that the final step in the catalytic cycle for total methane oxidation over CeO_2(1 1 1) is $[4H^* \rightarrow 2H_2O(g) + 2V_{\ddot{O}}]$ with $\Delta E = +4.6$ eV [18]. Their analysis of methane oxidation does not consider the complete catalytic cycle by neglecting oxygen vacancy filling and implies that the rate-determining step for methane oxidation over ceria is water formation with an apparent barrier of nearly 450 kJ/mol (+4.6 eV). Our method of incorporating elementary steps for water formation into the reaction energy diagram for methane oxidation represents continuous water formation from H* during the overall reaction.

2.4. Methane activation barriers

The majority of our analysis compares elementary reaction energies between surfaces. Activation barriers were computed for only C–H bond activation of methane. We do not calculate energy barriers for any reaction step following methane activation, as Knapp et al. show that the energy barrier for each C–H breaking step subsequent to methane activation is lower than the barrier for methane activation over the clean CeO_2(1 1 1) surface [18]. We use a 3 × 3 unit cell to calculate the methane activation barrier on Pd(1 1 1) to accommodate both CH_3 and H within the unit cell. The climbing image nudged elastic band method (CI-NEB) [46–48] was used to isolate transition states and calculate reaction energy barriers for methane activation ($CH_4(g) \rightarrow CH_3^* + H^*$). Within the CI-NEB method, a sequence of images along the reaction path are optimized with the highest energy image required to climb up in energy along the elastic band to estimate the saddle point along the minimum energy path [47]. Four equally spaced images between reactant and product states were used in each search (six images total), and transition states were identified as the maximum energy image with an absolute tangential force of less than 0.04 eV Å^{-1}.

3. Results and discussion

3.1. Reaction free energy diagrams for methane oxidation

The reaction free energy of each elementary step in methane oxidation over each surface is calculated at 0 K as well as at catalytic combustion conditions. Each reaction free energy diagram presented herein is calculated at $T = 298$ K and $P_{CH_4} = 0.01$ atm, $P_{O_2} = 0.04$ atm, $P_{H_2O} = P_{CO_2} = 10^{-6}$ atm, to represent typical experimental catalytic combustion conditions at 0% conversion [8,49]. Reaction free energies are calculated at $T = 298$ K as this temperature corresponds to the low conversion (low T) region of the methane oxidation light-off curve over CeO_2 [49,50]. The methane activation barriers displayed in each reaction free energy diagram are calculated as the Gibbs free energy of activation ($\Delta^{\ddagger}G$) at these catalytic combustion conditions, relative to the free energy of CH_4(g):

$$\Delta^{\ddagger}G = G_{TS^-}(G_{CH_4(g)} + G^*) \quad (4)$$

In each reaction energy diagram presented herein, intermediate energies are referenced to the free energy of $CH_4(g) + 2O_2(g)$. Table 1 displays the barriers at 0 K (E_{act}) and the standard Gibbs free energy of activation $\Delta^{\ddagger}G^0$ (at 273 K and $P_{CH_4} = 1.0$ atm) for methane activation on each surface. Table 2 displays the reaction free energies for each step in methane oxidation at 0 K. Adsorption geometries for all adsorbates on each surface are provided in the Supplementary material. The reaction free energy diagram for methane oxidation on Pd*/CeO_2(1 1 1) is also included in the Supplementary material.

3.1.1. Methane oxidation on CeO_2(1 1 1)

Fig. 2 displays the reaction free energy diagram for methane oxidation on CeO_2(1 1 1) at catalytic combustion conditions.

Methane adsorption on CeO_2(1 1 1) proceeds through H abstraction by a surface oxygen atom to form a methyl radical ($^{\cdot}CH_3$), followed by adsorption of $^{\cdot}CH_3$ [38]. Fig. 3a displays the transition state for methane activation on CeO_2(1 1 1). The methane activation barrier over CeO_2(1 1 1) is +1.65 eV

Table 1
Activation barriers at 0 K, free energies of activation at catalytic combustion conditions, relative combustion rate (normalized to the rate over CeO_2(1 1 1)), and stable intermediates for methane oxidation over CeO_2(1 1 1), $Pd_xCe_{1-x}O_2$(1 1 1), PdO(1 0 0), Pd(1 1 1), and Pd*/CeO_2(1 1 1).

Surface	0 K E_{act} (eV)	$\Delta^{\ddagger}G^0$ (eV)[a]	Relative combustion rate	Most stable intermediate
CeO_2(1 1 1)	+1.65	+1.88	1 (normalized)	HCO* (HCOO*)
$Pd_xCe_{1-x}O_2$(1 1 1)	+0.18	+0.53	6.97×10^{22}	H* (–OH)
PdO(1 0 0)	+1.08	+1.41	8.97×10^{7}	HCO* (HCOO*)
PdO(1 0 1)[55]	+0.65	+0.98[b]	1.69×10^{15}	–
Pd*/CeO_2(1 1 1)	+1.30	+1.70	1.11×10^{3}	CO*
Pd(1 1 1)	+0.89	+1.32	2.99×10^{9}	CH_3^* (–OCH_3)
Pd(1 1 1)	+0.66	+0.99[b]	1.15×10^{15}	–
Pd step[56]	+0.38	+0.71[b]	6.28×10^{19}	–
Pd kink[56]	+0.41	+0.74[b]	1.95×10^{19}	–

[a] Calculated at 273 K, $P_{CH_4} = 1$ atm.
[b] $\Delta^{\ddagger}S^0$ approximated at 0.33 eV.

Table 2
Reaction energies at 0 K for each elementary step in methane oxidation over CeO_2(1 1 1), $Pd_xCe_{1-x}O_2$(1 1 1), and PdO(1 0 0).

CeO_2(1 1 1)	0 K ΔE (eV)	PdO(1 0 0)	0 K ΔE (eV)
$CH_4(g) \rightarrow CH_3^* + H^*$	−0.81	$CH_4(g) \rightarrow CH_3^* + H^*$	−1.05
$CH_3^* \rightarrow CH_2^* + H^*$	+0.51	$CH_3^* \rightarrow CH_2^* + H^*$	−0.67
$CH_2^* \rightarrow CH^* + H^*$	+0.19	$CH_2^* \rightarrow CH^* + H^*$	−0.06
$CH^* \rightarrow HCO^*$	−1.82	$^*CH \rightarrow {}^*HCO$	−0.75
$HCO^* \rightarrow CO^* + H^*$	+0.78	$HCO^* \rightarrow CO^* + H^*$	+0.29
$CO^* \rightarrow CO_2(g)$	−0.18	$CO^* \rightarrow CO_2(g)$	−1.01
$Pd_xCe_{1-x}O_2$(1 1 1)			
$CH_4(g) \rightarrow CH_3^* + H^*$	−2.29		
$CH_3^* \rightarrow CH_2^* + H^*$	−2.05		
$CH_2^* \rightarrow CH^* + H^*$	−0.96		
$^*CH \rightarrow {}^*HCO$	−1.58		
$HCO^* \rightarrow CO^* + H^*$	−1.94		
$CO^* \rightarrow CO_2(g)$	+0.60		

($\Delta^{\ddagger}G^0$ = +2.05 eV at 298 K), with the ($\cdot CH_3 + *H$) state 0.2 eV lower in energy (+1.40 eV at 0 K [38], +1.85 eV at 298 K) than the transition state. Our previous study reported the energy of ($\cdot CH_3 + H^*$) as the highest energy state between CH_4(g) and $CH_3^* + H^*$ [38]; however, subsequent finer searches along the reaction coordinate identified this higher-energy transition state. This transition state for methane activation over CeO_2(1 1 1) has a single imaginary vibrational frequency along the reaction coordinate (in contrast to the absence of a imaginary frequency in the transition state reported previously [38]), an absolute tangential force of less than 0.04 eV Å^{-1}, and forces on all atoms below 0.05 eV Å^{-1}. This transition state precedes the $\cdot CH_3 + H^*$ state along the reaction coordinate, with the C–H bond elongated and the O–H bond partially formed. The reaction free energy for ($CH_4(g) \rightarrow CH_3^* + H^*$) is slightly exergonic at −0.14 eV; however, each subsequent C–H breaking step over pure ceria is endergonic (with the most endergonic step $HCO^* \rightarrow CO^* \rightarrow H^*$ at +0.71 eV). Each water formation step ($^*H \rightarrow \frac{1}{2}H_2O(g) + \frac{1}{2}V_{\ddot{o}} + \frac{1}{2}*$) over ceria is endergonic by +0.45 eV, and each oxygen vacancy filling step ($\frac{1}{4}O_2 + \frac{1}{2}V_{\ddot{o}} \rightarrow \frac{1}{2}*$) is exergonic by −2.44 eV (−4.88 eV per $V_{\ddot{o}}$). Methane activation over the hydroxylated surface was not considered as the barrier would be expected to increase. We instead presume that water desorption and vacancy refilling by oxygen must precede C–H activation in the catalytic cycle.

Each CH_x species ($1 \leqslant x \leqslant 3$) adsorbs atop a surface oxygen atom on CeO_2(1 1 1), with elongation of each adjacent Ce–O bond. The lowest energy path of methane oxidation proceeds over CeO_2(1 1 1) by breaking the first three C–H bonds to form CH*, oxidizing to HCO*, breaking the final C–H bond to form CO*, which desorbs as CO_2(g) leaving an oxygen vacancy. Carbon monoxide binds weakly atop a Ce atom and is easily oxidized on CeO_2(1 1 1), as evidenced by the favorable free energy of −1.04 eV at 298 K for $CO^* \rightarrow CO_2(g) + 2H_2O(g) + V_{\ddot{o}}$. This result is similar to the findings of previous DFT + U studies of CO adsorption on ceria [51,52]. Carbon dioxide adsorption to CeO_2(1 1 1) is equivalent to CO_3^{2-} formation on an oxygen vacancy. However, carbonate formation is not preferable as it is more exergonic for CO* to desorb as CO_2(g) (−1.04 eV at 298 K) than to form CO_2^* (−0.61 eV at 298 K). Intermediates including CH_3O^*, CH_3OH^*, H_2CO^*, H_2COH^*, HCOH*, C*, and HCOO* were also considered. The formation of each of these was endergonic with respect to other intermediates along the lowest energy path.

Stable intermediates along the lowest energy path were identified as those for which the subsequent reaction step is uphill (endergonic) in free energy. The "most stable intermediate" is identified as the intermediate from which the subsequent reaction step in the most endergonic. The most stable intermediate over CeO_2(1 1 1) is HCO*, which adsorbs with the carbon atom atop a surface oxygen, and is equivalent to formate ($HCOO^-$) adsorbed atop an oxygen vacancy. Diffuse reflection infrared Fourier transform spectroscopy (DRIFTS) analysis confirmed the presence and stability of surface formates on ceria during low-temperature water–gas shift reaction conditions [53,54]. These DRIFTS studies determine the stretching bands for formate on ceria to be 2950 cm^{-1} for C–H stretch and 1580 cm^{-1} for O–C–O asymmetric stretching [53,54]; we calculate 2970 cm^{-1} for C–H stretch and 1599 cm^{-1} for O–C–O asymmetric stretching. Stable intermediates other than HCO* on CeO_2(1 1 1) include CH_3^*, CH_2^*, and H*. The stability of CH_3^* and CH_2^* is further evidence of C–H breaking activity as the limiting factor in hydrocarbon oxidation activity. The stability of H* suggests that hydroxyl groups will be present on the ceria surface during reaction. The formation energies of partial oxidation

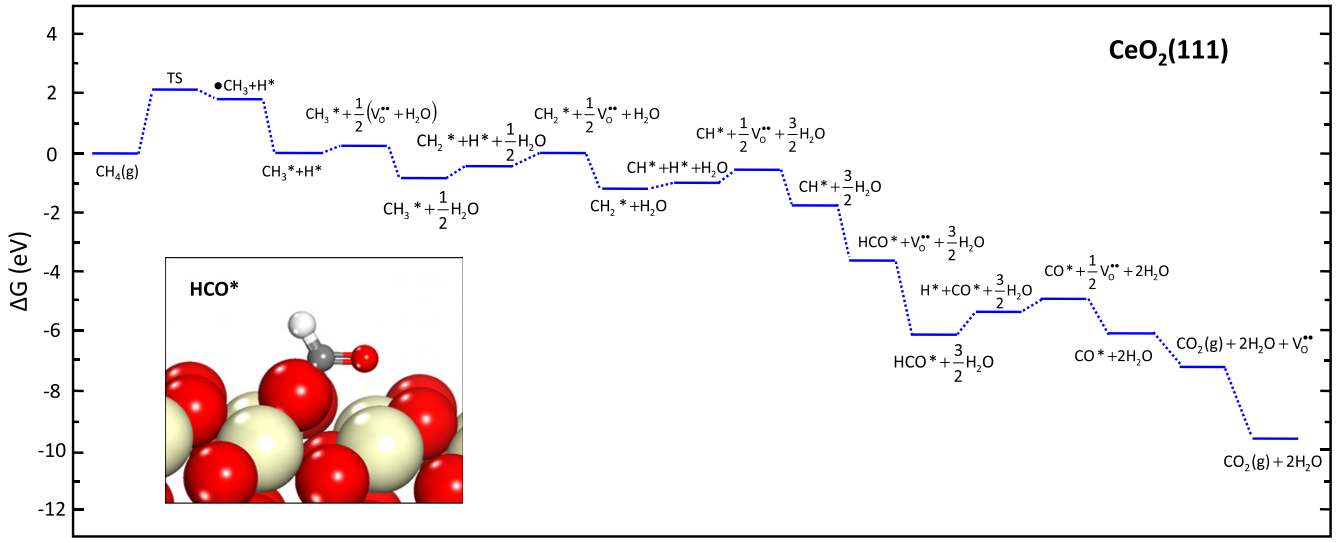

Fig. 2. Reaction free energy diagram for $CH_4(g) + 2O_2(g) \rightarrow CO_2(g) + 2H_2O(g)$ over CeO_2(1 1 1) at T = 298 K and P_{CH_4} = 0.01 atm, P_{O_2} = 0.04 atm, $P_{H_2O} = P_{CO_2}$ = 10–6 atm. Inset: HCO* ($HCOO^-$), the most stable intermediate in methane oxidation over CeO_2(1 1 1). Ce is displayed as tan (light), O as red (dark), C as gray, and H as white. Oxygen (O_2) is not explicitly included in the oxidation mechanism, as addition of O_2 to the surface occurs in oxygen vacancy filling steps. (For interpretation of the references to colour in this figure legend, the reader is referred to the web version of this article.)

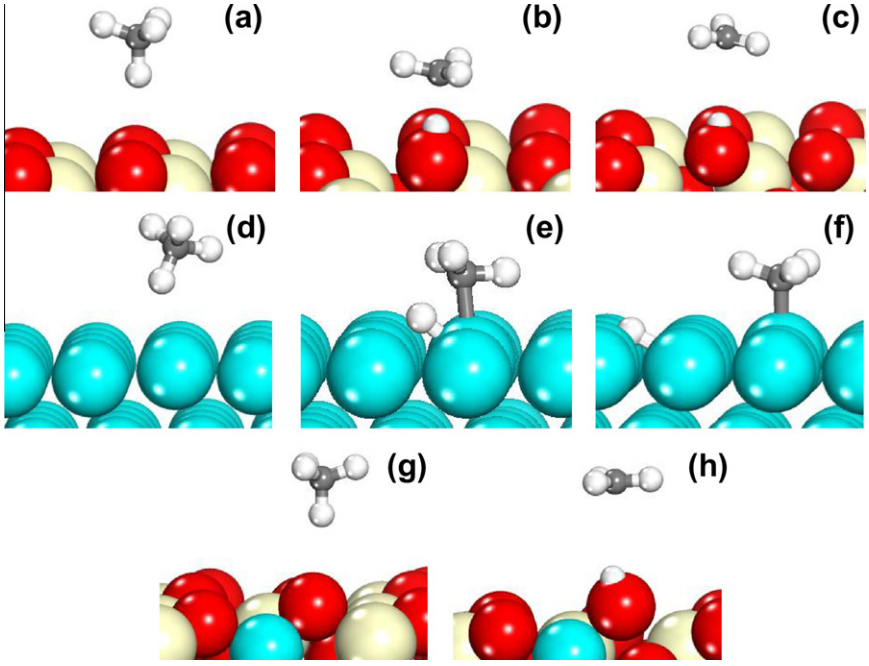

Fig. 3. Initial (a, d, g), transition (b, e), and final (c, f, h) states for methane activation on CeO_2(1 1 1) (a, b, c), Pd(1 1 1) (d, e, f), and $Pd_xCe_{1-x}O_2$(1 1 1) (g, h). Ce is displayed as tan (light), Pd as light blue (gray), O as red (dark), C as gray, and H as white. (For interpretation of the references to colour in this figure legend, the reader is referred to the web version of this article.)

products such as methanol (CH_3OH), formaldehyde (H_2CO), and formic acid (H_2COOH) were thermodynamically unfavorable at both 0 K and catalytic combustion conditions compared to further steps toward total oxidation (CO_2) and thus are not included in the minimum energy path over CeO_2(1 1 1).

3.1.2. Methane oxidation on $Pd_xCe_{1-x}O_2$(1 1 1)

Fig. 4 displays the reaction free energy diagram for methane oxidation on $Pd_xCe_{1-x}O_2$(1 1 1) at catalytic combustion conditions. Methane adsorption on $Pd_xCe_{1-x}O_2$ proceeds through H abstraction by a surface oxygen atom to form $\cdot CH_3$, followed by adsorption of CH_3 [38]. Subsequent finer searches along the reaction coordinate over $Pd_xCe_{1-x}O_2$(1 1 1) (equivalent to our approach over CeO_2(1 1 1)) indicated a monotonic increase in energy between CH_4(g) and ($\cdot CH_3 + H^*$), in contrast to the higher-energy transition state between these two states found on pure ceria. The free energy ($\Delta^{\ddagger}G$) of the ($\cdot CH_3 + H^*$) state over $Pd_xCe_{1-x}O_2$(1 1 1) is +0.70 eV (E_{act} = +0.18 eV at 0 K [38]) with respect to CH_4(g), substantially lower than that over pure ceria ($\Delta^{\ddagger}G$ = +1.85 eV, E_{act} = +1.40 eV at 0 K).

Each C–H breaking step over $Pd_xCe_{1-x}O_{2(1\,1\,1)}$ is more exergonic than the corresponding step over CeO_2(1 1 1). The minimum energy path on $Pd_xCe_{1-x}O_2$(1 1 1) follows the same intermediates as for methane oxidation on CeO_2(1 1 1) (i.e. C–H breaking to CH^*, C–O forming to HCO^*, C–H breaking to CO^*, then desorption as $CO_2 + V_{\ddot{O}}$). Carbon dioxide adsorbs equivalent to CO_3^{2-} on an oxygen vacancy on $Pd_xCe_{1-x}O_2$(1 1 1); however, it is exergonic for CO^* to desorb as CO_2(g) (−0.34 eV at 298 K), whereas the formation of CO_2^* is endergonic (+0.13 eV at 298 K). Each CH_x species ($1 \leqslant x \leqslant 3$) adsorbs atop a surface oxygen atom on $Pd_xCe_{1-x}O_2$(1 1 1), with elongation of adjacent Pd–O and Ce–O bonds. Our previous study of Pd-substituted ceria surfaces highlighted that Pd substitution increases surface reducibility with respect to pure ceria and thereby provides more active surface oxygen for oxidation reactions. Adsorption of CH_x and H on the $Pd_xCe_{1-x}O_2$(1 1 1) surface results in reduction of the incorporated Pd^{4+} species, which is more exothermic than reduction of Ce^{4+} [38]. In the bare $Pd_xCe_{1-x}O_2$(1 1 1) surface, Pd^{4+} is approximately octahedrally coordinated by O atoms, as expected based on crystal field theory arguments for the d^6 metal center. Upon adsorption of H or CH_x fragments, Pd–O bonds lengthen, and specifically, elongation of a Pd–O subsurface bond provides for a nearly square planar O environment about the d^8 Pd^{2+} atom. The Pd atom therefore provides the reduction center, and incorporation into the CeO_2 lattice provides for structural flexibility to stabilize both the Pd^{4+} and Pd^{2+} states.

The most stable intermediate over $Pd_xCe_{1-x}O_2$(1 1 1) is H^*, as the only endergonic reaction steps following methane activation are water formation steps. The formation energies of partial oxidation products such as methanol (CH_3OH), formaldehyde (H_2CO), and formic acid (H_2COOH) were more endergonic than further steps toward total oxidation (CO_2) and thus are not included in the minimum energy path over $Pd_xCe_{1-x}O_2$(1 1 1).

3.1.3. Methane oxidation on PdO(1 0 0)

Though the low methane activation barrier over $Pd_xCe_{1-x}O_2$(1 1 1) suggests that incorporated Pd^{4+} ions in ceria provide high activity for methane oxidation, it is possible that the active cationic Pd species identified experimentally correspond to PdO_x clusters. We use the PdO(1 0 0) surface to approximate the surface of a PdO particle because the surface formation energy of the (1 0 0) termination of PdO is less endergonic than all other single crystal terminations of PdO at O_2 pressures above 10^{-30} atm at 300 K [45]. Fig. 5 displays the reaction energy diagram for methane oxidation on PdO(1 0 0) at catalytic combustion conditions. Methane adsorption on PdO(1 0 0) occurs dissociatively with CH_3 and H fragments adsorbing atop surface oxygen atoms, similar to methane dissociative adsorption on pure ceria [38]. Searches along the reaction coordinate over PdO(1 0 0) indicated a monotonic increase in energy between CH_4(g) and ($\cdot CH_3 + H^*$), and we approximate the energy barrier for methane activation on PdO(1 0 0) as the energy of $CH_4 \rightarrow \cdot CH_3 + H^*$ (H abstraction and methyl radical formation). Product or transition states that involved interaction of H and CH_3 fragments with surface Pd^{2+} were higher in energy than that of H^* and CH_3^* atop surface oxygen atoms. The free energy

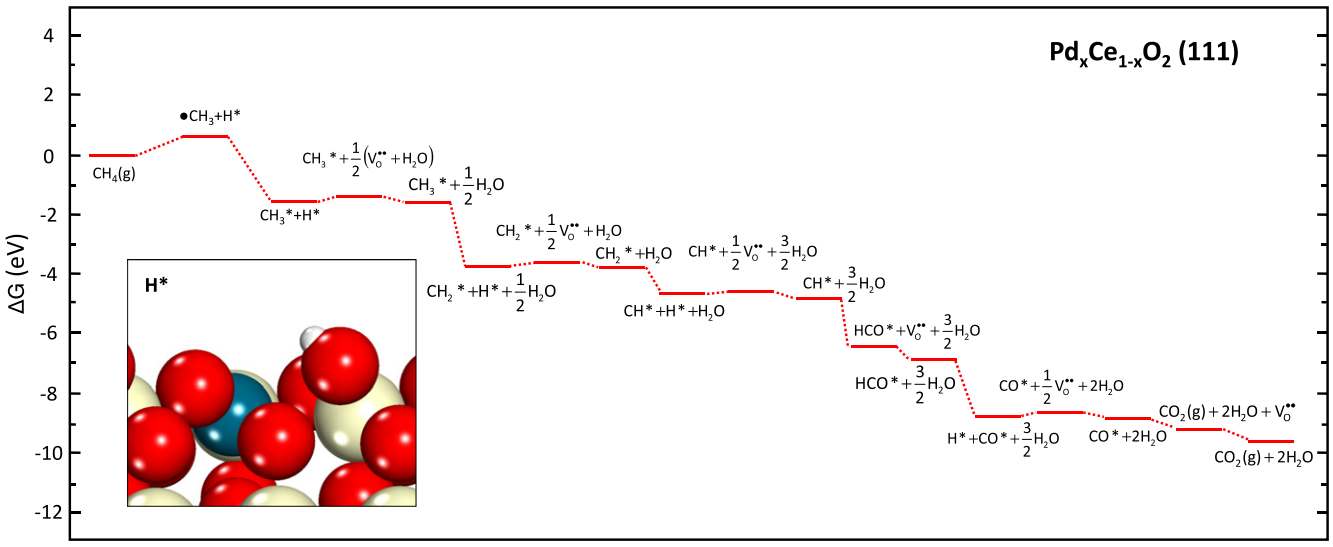

Fig. 4. Reaction free energy diagram for $CH_4(g) + 2O_2(g) \rightarrow CO_2(g) + 2H_2O(g)$ over $Pd_xCe_{1-x}O_2(1\,1\,1)$ at $T = 298$ K and $P_{CH_4} = 0.01$ atm, $P_{O_2} = 0.04$ atm, $P_{H_2O} = P_{CO_2} = 10^{-6}$ atm. Inset: H* (–OH), the most stable intermediate in methane oxidation over $Pd_xCe_{1-x}O_2(1\,1\,1)$. Ce is displayed as tan (light), Pd as light blue (gray), O as red (dark), and H as white. (For interpretation of the references to colour in this figure legend, the reader is referred to the web version of this article.)

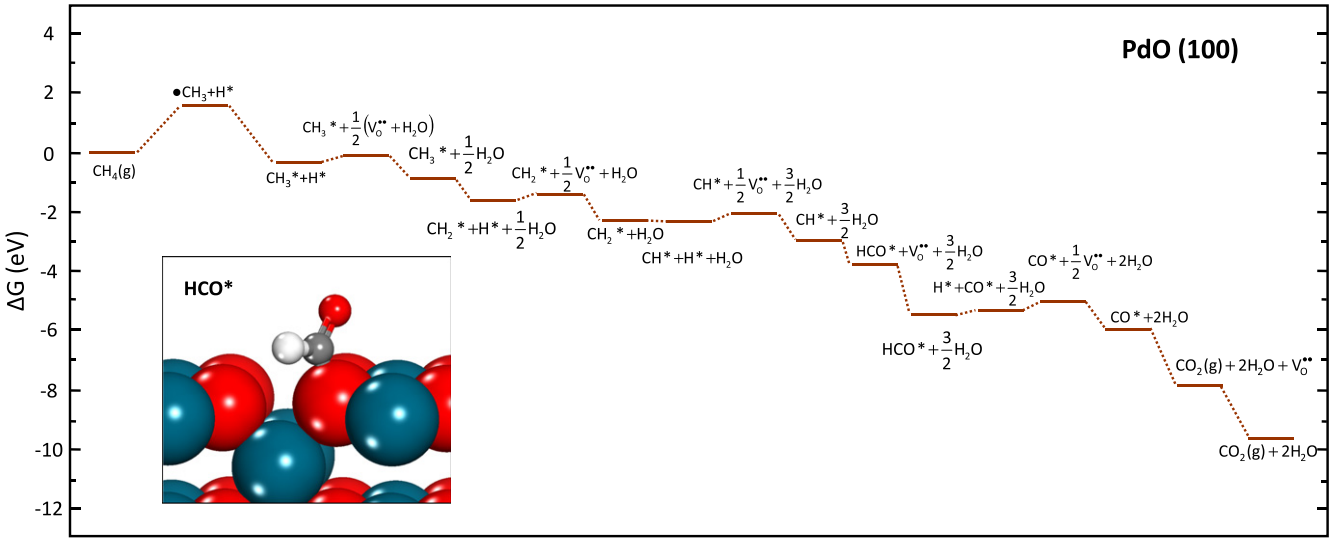

Fig. 5. Reaction free energy diagram for $CH_4(g) + 2O_2(g) \rightarrow CO_2(g) + 2H_2O(g)$ over PdO(1 0 0) at $T = 298$ K and $P_{CH_4} = 0.01$ atm, $P_{O_2} = 0.04$ atm, $P_{H_2O} = P_{CO_2} = 10^{-6}$ atm. Inset: HCO* ($HCOO^-$), the most stable intermediate in methane oxidation over PdO(1 0 0). Pd is displayed as light blue (gray), O as red (dark), C as gray, and H as white. (For interpretation of the references to colour in this figure legend, the reader is referred to the web version of this article.)

of the $^{\cdot}CH_3$ + H* state ($\Delta^{\ddagger}G$) is +1.58 eV (+1.08 eV at 0 K), lower than over pure ceria and Pd*/CeO_2(1 1 1), but higher than that over $Pd_xCe_{1-x}O_2$(1 1 1).

Methane activation on PdO may also occur over coordinatively unsaturated Pd atoms, either present near oxygen vacancies or present on surfaces terminated by Pd with less than six-fold oxygen coordination. Weaver et al. reported a DFT calculated methane activation barrier of 0.65 eV on PdO(1 0 1) at 0 K via metal insertion of a coordinatively unsaturated surface Pd atom [55]. Methane dissociation over an oxygen vacancy on Pd(1 0 0) is endergonic at +0.03 eV at 298 K, 0.4 eV more endergonic than over the stoichiometric surface (−0.37 eV at 298 K). The more endergonic methane dissociation energy over PdO(1 0 0)/$V_{\ddot{O}}$ suggests that methane activation over oxygen vacancies on PdO(1 0 0) is not favorable relative to activation by H abstraction over the stoichiometric surface. Methane activation transition state searches over PdO(1 0 0)/$V_{\ddot{O}}$ indicate that activation via metal insertion does not stabilize a transition state lower in energy than activation via H abstraction over the intact PdO(1 0 0) surface. The activation barrier and transition state over PdO(1 0 1) illustrate, however, that methane activation can be facile over PdO surface terminations which expose unsaturated Pd atoms of specific coordination and geometry and that the methane activation barrier on PdO via metal insertion is lower than via H abstraction on PdO(1 0 0).

Each C–H breaking step over PdO(1 0 0) is exergonic, with the exception of HCO* → CO*. Every C–H breaking step subsequent to $CH_4 \rightarrow CH_3^* + H^*$ is more exergonic than over CeO_2(1 1 1), but less exergonic than over Pd*/CeO_2(1 1 1) or $Pd_xCe_{1-x}O_2$(1 1 1). The minimum energy path on PdO(1 0 0) follows the same intermediates as on each ceria surface, and each adsorbate sits atop one surface O atom or bridged between two surface O atoms. The most stable intermediate is CO*, which binds strongly at a site bridging

between two surface oxygen and is equivalent to a carbonate ion, CO_3^{2-}, adsorbed on two adjacent oxygen vacancies. This adsorption mode for CO^* is also equivalent to CO_2 adsorbed on a single oxygen vacancy; no stable adsorption site was found for CO_2 on the intact PdO(1 0 0) surface. The vacancy formation energy on PdO(1 0 0) (+2.16 eV at 0 K) is less than that on CeO_2(1 1 1) (+2.76 eV at 0 K) or Pd^*/CeO_2(1 1 1) (+2.64 eV at 0 K), and thus, water formation is more exergonic and oxygen vacancy filling is more endergonic on PdO than over CeO_2(1 1 1) or Pd^*/CeO_2(1 1 1). The formation of partial oxidation products was prohibitively endergonic as found for ceria-based surfaces.

3.1.4. Methane activation on Pd metal sites

Though the barrier for methane activation on $Pd_xCe_{1-x}O_2$(1 1 1) is less than that for CeO_2(1 1 1) or PdO(1 0 0), it is possible that reduced metal (Pd^0) sites provide greater methane oxidation activity. Hu et al. calculate the barrier over Pd(1 1 1) as 0.66 eV, with the barrier over a Pd surface step (Pd(2 1 1)) as + 0.38 eV and over a Pd surface kink (Pd vacancy on Pd(2 1 1)) as + 0.41 eV [56]. With the same methods as used herein, we calculate the methane activation barrier over Pd(1 1 1) in a 3×3 unit cell to be +0.89 eV. All of the values are significantly higher than the barrier of 0.18 eV determined for methane activation over $Pd_xCe_{1-x}O_2$(1 1 1). We also considered methane activation over a single Pd adatom on ceria (Pd^*/CeO_2(1 1 1)), as an extreme case for ideally dispersed palladium on ceria. The methane activation barrier is +1.30 eV on Pd^*/CeO_2(1 1 1), higher than on $Pd_xCe_{1-x}O_2$(1 1 1), PdO(1 0 0), or Pd metal surfaces. Adsorbed oxygen (O^*) will be present on the Pd surface during reaction, and methane activation may also occur over O^* species. Preliminary calculations indicate that the methane activation reaction energy and barrier are higher over oxygen-covered Pd(1 1 1) than over Pd(1 1 1) or Pd steps or kinks.

Further description of the Pd(1 1 1) and Pd^*/CeO_2(1 1 1) surface models as well as full analysis of the methane oxidation reaction mechanism over each surface is included in the Supplementary material.

3.2. Dependence of rate-determining steps on operating conditions

We compare operating regimes for the catalytic combustion of methane and methane electro-oxidation in a SOFC within which distinct elementary steps over each surface are rate determining (provide the largest energy barrier). The free energy of methane activation ($\Delta^{\ddagger}G$), as well as the free energies of product desorption steps, is a function of temperature and the partial pressures of reactants and products, and thus, the rate-determining step is also a function of temperature and partial pressures. For example, at very high pressures of H_2O(g) product, the desorption of H_2O may be more endergonic than any other elementary reaction energy or barrier. At low O_2 pressures, oxygen vacancy filling will become rate limiting. The $\Delta^{\ddagger}G$ for methane activation is also dependent on the methane pressure, with higher pressures reducing $\Delta^{\ddagger}G$. We implement Murdoch's procedure [57] to identify the rate-determining step of methane oxidation within each operating regime. Murdoch's procedure involves dividing the reaction free energy diagram into sections of steadily decreasing free energy and identifying the reaction sequence that passes through the largest ΔG barrier of any given section as the rate-determining step [57].

The partial pressures of reactants and products used to represent catalytic combustion reactor conditions at conversions greater than 0% were fixed by the stoichiometry of the overall reaction. SOFC conditions were set as 973 K, 1 atm CH_4 at the anode (pure methane anode feed), and 0.21 atm O_2 at the cathode (air cathode feed), equivalent to experimental conditions in previous studies of direct oxidation of hydrocarbons in SOFCs [58–60]. The partial pressure of O_2 at the anode was fixed by the cell potential by the Nernst relationship:

$$E = \left[\frac{RT}{2F}\right] \ln \left[\frac{\left(P_{O_2}^{cathode}\right)^{\frac{1}{2}}}{\left(P_{O_2}^{anode}\right)^{\frac{1}{2}}}\right] \tag{5}$$

where the cell potential E is set at the equilibrium potential of 1.05 V (@973 K) for 0% conversion [59]. The partial pressures of H_2O and CO_2 at the anode are also fixed by the Nernst relationship, which can be rewritten for methane oxidation as:

$$E = E^0 + \left[\frac{RT}{8F}\right] \ln \left[\frac{\left(P_{CH_4}^{anode}\right) \cdot \left(P_{O_2}^{cathode}\right)^2}{\left(P_{H_2O}^{anode}\right)^2 \cdot \left(P_{CO_2}^{anode}\right)}\right] \tag{6}$$

where $P_{H_2O}^{anode}$, $P_{CO_2}^{anode}$, $P_{CH_4}^{anode}$, and $P_{O_2}^{cathode}$ values at conversions greater than 0% are fixed by the stoichiometry of the overall reaction.

Fig. 6 depicts the regions of O_2 and H_2O partial pressures within which either of the following segments of the methane oxidation path over CeO_2(1 1 1) is rate determining:

$$\text{(A)}\quad CH_4(g) \rightarrow {}^{\cdot}CH_3 + H^* \rightarrow {}^{\cdot}CH_3^* + H^*$$

$$\text{(B)}\quad HCO^* + * \rightarrow H^* + CO^* \rightarrow CO^* + \frac{1}{2}H_2O(g) + \frac{1}{2}V_{\ddot{O}} + \frac{1}{2}*$$

$$\text{(C)}\quad HCO^* + * \rightarrow H^* + CO^* \rightarrow CO^* + \frac{1}{2}H_2O(g) + \frac{1}{2}V_{\ddot{O}} + \frac{1}{2}* \rightarrow CO^* + \frac{1}{2}H_2O(g) + *$$

Segments B and C represent H_2O formation and vacancy filling, respectively, each referenced to HCO^* since it is the most stable intermediate over CeO_2(1 1 1). At catalytic combustion conditions (Fig. 6a), methane oxidation on CeO_2(1 1 1) is rate limited by CH_4 activation at all conversions. The regions of O_2 and H_2O pressures within which water formation or vacancy filling is endergonic to the extent that the rate-determining step is altered are characterized by extremely low O_2 pressures ($<10^{-80}$ atm) and extremely high H_2O pressures ($>10^{20}$ atm). At SOFC conditions, methane oxidation over ceria is also rate limited by CH_4 activation; however, the region within which vacancy filling contributes to the rate-determining step is much larger at the higher SOFC temperature; the free energy of O_2(g) is lower and thus vacancy filling is more endergonic at higher temperatures.

Over $Pd_xCe_{1-x}O_2$(1 1 1), the methane activation barrier is lower than over CeO_2(1 1 1), and therefore, the conditions over which H_2O desorption or vacancy filling are limiting may be expected to vary. Fig. 7 depicts the regions of O_2 and H_2O partial pressures within which methane activation, water formation, or vacancy filling over $Pd_xCe_{1-x}O_2$(1 1 1) is rate determining. Methane activation is more exergonic over $Pd_xCe_{1-x}O_2$(1 1 1) than over CeO_2(1 1 1), which contracts the region within which methane activation is rate determining. Although this region is contracted, methane oxidation remains rate limited by CH_4 activation at all conditions of interest over $Pd_xCe_{1-x}O_2$(1 1 1). The regions of H_2O and O_2 pressures within which water formation and/or vacancy filling are rate determining over $Pd_xCe_{1-x}O_2$(1 1 1) are characterized by lower H_2O pressures and higher O_2 pressures than over CeO_2(1 1 1), because the $Pd_xCe_{1-x}O_2$(1 1 1) surface is more reducible.

The comparison of rate-determining regions on $Pd_xCe_{1-x}O_2$(1 1 1) versus CeO_2(1 1 1) illustrates the trade-off in the development of ceria-based mixed oxide catalysts between surface reducibility and C–H bond activity as established in our previous study [38]. The incorporation of Pd^{4+} ions into the CeO_2 lattice increases the reducibility of the ceria surface and thereby the catalytic activity for methane oxidation. Though the trade-off is that increased reducibility will make vacancy filling more difficult,

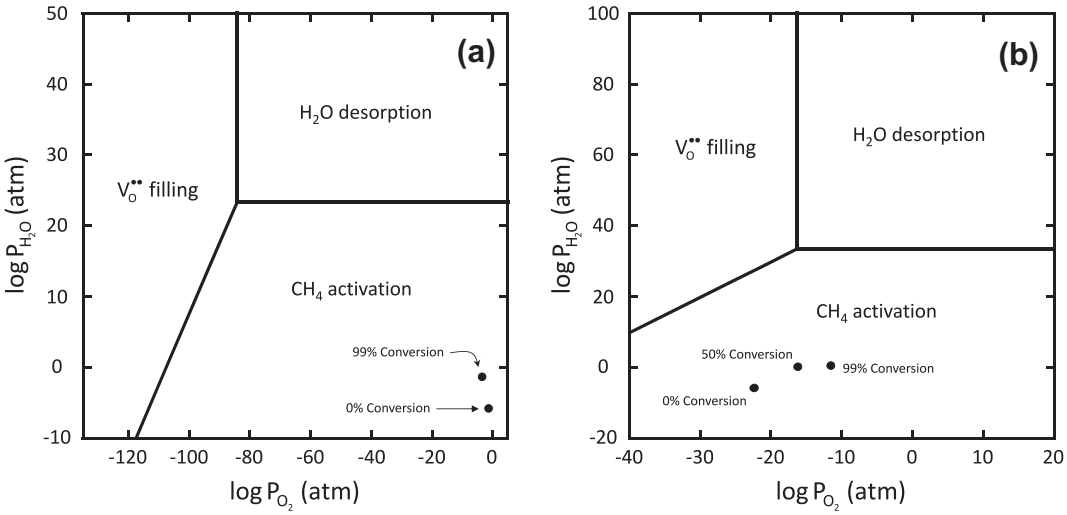

Fig. 6. Phase regions of rate-determining steps of methane oxidation over CeO_2(1 1 1) at 298 K/catalytic combustion operating conditions (a) and 973 K/SOFC conditions (b). Filled circles (●) represent conditions at the labeled conversions for (a) 298 K/catalytic combustion and (b) 973 K/SOFC.

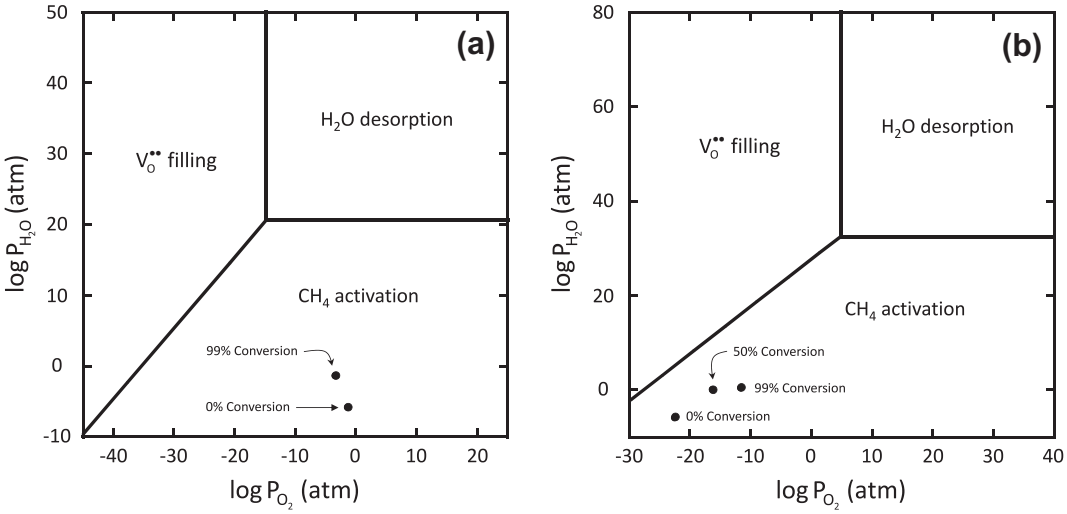

Fig. 7. Phase regions of rate-determining steps of methane oxidation over $Pd_xCe_{1-x}O_2$(1 1 1) at 298 K/catalytic combustion operating conditions (a) and 973 K/SOFC conditions (b). Filled circles (●) represent conditions at the labeled conversions for (a) 298 K/catalytic combustion and (b) 973 K/SOFC.

vacancy filling is rate determining only at very low O_2 ($<10^{-30}$ atm) pressures at both 298 K and 973 K, suggesting that the catalysis of hydrocarbon oxidation by ceria-based oxides is only dependent on the energetics of C–H activation.

Plots depicting the dependence of rate-determining steps on operating pressures at 298 K and 973 K for methane oxidation over PdO(1 0 0), Pd(1 1 1), and Pd^*/CeO_2(1 1 1) are included in the Supplementary material. At both 298 K and 973 K, methane oxidation is limited by C–H activation over PdO(1 0 0), Pd(1 1 1), and Pd^*/CeO_2(1 1 1) at all conversions.

4. Conclusions

The DFT + *U* method was used to calculate the free energies of elementary methane oxidation reaction steps over pure CeO_2(1 1 1), $Pd_xCe_{1-x}O_2$(1 1 1), and PdO(1 0 0). Methane oxidation over Pd/ceria is limited by C–H activation, the barrier of which is affected by the oxidation state, morphology, and chemical composition of the surface. At low coverage, methane oxidation occurs over each surface via C–H breaking steps to CH^*, C–O forming to form HCO^* (equivalent to $HCOO^-$ atop an oxygen defect for each oxide surface), subsequent C–H breaking to CO^*, and finally C–O formation and desorption as CO_2(g). The formation of C^* is not favored over any surface, suggesting that, under the reaction conditions considered, deactivation due to the formation of carbon deposits is not likely. The formation of partial oxidation products is also not thermodynamically favorable, which is in agreement with the selectivity of ceria, palladium, and palladium/ceria for the complete oxidation of CH_4 to CO_2.

Table 1 lists the activation barrier, relative combustion rate, and most stable intermediate over each surface considered. Rate constants were calculated as:

$$k = \frac{k_B T}{h} e^{\frac{-\Delta^{\ddagger} G^0}{RT}} \tag{7}$$

where k_B is Boltzmann's constant, T is temperature, h is Planck's constant, R is the universal gas constant, and $\Delta^{\ddagger}G^0$ is the standard free energy of activation. The relative combustion rates listed in Table 1 are the ratios of the rate constant over each surface to the rate constant over CeO_2(1 1 1). Methane activation is rate determining over each surface, at both catalytic combustion and SOFC operating

conditions. The methane activation barrier is lowest over $Pd_xCe_{1-x}O_2(1\,1\,1)$, lower than that over Pd(1 1 1), stepped Pd(2 1 1) [56], kinked Pd(2 1 1) [56], PdO(1 0 0), $Pd^*/CeO_2(1\,1\,1)$, and $CeO_2(1\,1\,1)$. The relative rate of methane oxidation over $Pd_xCe_{1-x}O_2(1\,1\,1)$ is three orders of magnitude larger than that over stepped Pd(1 1 1) and much larger (>13 orders of magnitude) than over Pd(1 1 1), $CeO_2(1\,1\,1)$, and PdO(1 0 0).

These results indicate that incorporated Pd^{4+} ions in ceria provide higher catalytic activity for methane oxidation than large Pd particles (Pd(1 1 1)) or large palladium oxide particles (PdO(1 0 0)). An actual Pd/ceria catalyst will contain a heterogeneous distribution of surface sites, particle sizes, and Pd oxidation states. The relative rate of methane oxidation over $Pd_xCe_{1-x}O_2(1\,1\,1)$ shows that, even if the concentration of incorporated Pd^{4+} atoms is 1000 times smaller than that of stepped or kinked sites on metallic particles, the rate of methane oxidation over incorporated Pd^{4+} will provide the majority of the overall reaction rate. Stable intermediates differ over incorporated Pd^{4+} versus Pd^0, Pd^{2+}, or CeO_2, and thus intermediates identified experimentally may correspond to those present on less active sites than Pd^{4+}.

Our models represent the limits of ideally dispersed Pd^{4+} and infinitely large Pd or PdO particles. Experimental studies establish the importance of Pd–O–Ce linkages and more generally oxidized Pd species in dictating the catalytic activity of Pd/ceria; however, these sites could exist on the edge of metal or PdO clusters. Consideration of all possible particle sizes and morphologies is computationally prohibitive, and it is possible that highly active sites at the boundary between PdO_x particles and the CeO_2 support could provide activity similar to incorporated $Pd_xCe_{1-x}O_2(1\,1\,1)$. This study illustrates that mixed noble metal–ceria oxides can provide enhanced activity for hydrocarbon oxidation by tuning the reducibility of the mixed noble metal–ceria surface and thereby the methane activation kinetics. These results provide insight into the catalytic activity and surface functionality of Pd/ceria for hydrocarbon oxidation and motivate future efforts in the development of noble metal–ceria mixed oxide catalysts.

Appendix A. Supplementary material

Supplementary data associated with this article can be found, in the online version, at doi:10.1016/j.jcat.2010.11.006.

References

[1] G. Zhou, P.R. Shah, T. Montini, P. Fornasiero, R. Gorte, Journal of Surface Science 601 (2007) 2512–2519.
[2] E. Aneggi, M. Boaro, C.d. Leitenburg, G. Dolcetti, A. Trovarelli, Journal of Alloys and Compounds 408-412 (2006) 1096–1102.
[3] A. Bensalem, F. Bozon-Verduraz, V. Perrichon, Journal of the Chemical Society, Faraday Transactions 91 (1995) 2185–2189.
[4] B. Wang, D. Weng, X. Wu, J. Fan, Catalysis Today 153 (2010) 111–117.
[5] S. Colussi, A. Gayen, M.F. Camellone, M. Boaro, J. Llorca, S. Fabris, A. Trovarelli, Angewandte Chemie International 48 (2009) 8481–8484.
[6] S. McIntosh, J.M. Vohs, R.J. Gorte, Electrochemical and Solid-State Letters 6 (2003) A240–A243.
[7] S.H. Oh, G.B. Hoflund, Journal of Physical Chemistry A 110 (2006) 7609–7613.
[8] L. Xiao, K. Sun, X. Xu, X. Li, Catalysis Communications 6 (2005) 796–801.
[9] A. Badri, C. Binet, J.C. Lavalley, Journal of the Chemical Society, Faraday Transactions 92 (1996) 1603–1608.
[10] G.W. Graham, H.W. Jen, R.W. McCabe, A.M. Straccia, L.P. Haack, Catalysis Letters 67 (2000) 99–105.
[11] H.W. Jen, G.W. Graham, W. Chun, R.W. McCabe, J.P. Cuif, S.E. Deutsch, O. Touret, Catalysis Today 50 (1999) 309–328.
[12] X.G. Wang RJ., J.P. Wagner, Journal of Catalysis 212 (2002) 225–230.
[13] A.D. Mayernick, M.J. Janik, Journal of Chemical Physics (2009) 131.
[14] J.H. Holles, R.J. Davis, T.M. Murray, J.M. Howe, Journal of Catalysis 195 (2000) 193–206.
[15] Y. Matsumura, W. Shen, Y. Ichihashi, H. Ando, Catalysis Letters 68 (2000) 181–183.
[16] W. Matsumura, Physical Chemistry Chemical Physics 2 (2000) 1519–1522.
[17] K.R. Priolkar, B. Parthasarathi, P.R. Sarode, M.S. Hegde, S. Emura, R. Kumashiro, N.P. Lalla, Chemistry of Materials 14 (2002) 2120–2128.
[18] D. Knapp, T. Ziegler, The Journal of Physical Chemistry C 112 (2008) 17311–17318.
[19] G.B. Hoflund, H.A.E. Hagelin, J.F. Weaver, G.N. Salaita, Applied Surface Science 205 (2003) 102–112.
[20] H. Zhang, J. Gromek, G. Fernando, H. Marcus, S. Boorse, Journal of Phase Equilibria and Diffusion 23 (2002) 246–248.
[21] J.H. Guanghui Zhu, Zemlyanov Dmitri Yu, Fabio H. Ribeiro, Journal of Physical Chemistry B 109 (2005) 2331–2337.
[22] D. Mei, N. Aaron Deskins, M. Dupuis, Surface Science 601 (2007) 4993–5001.
[23] C. Muller, C. Freysoldt, M. Baudin, K. Hermansson, Chemical Physics 318 (2005) 180–190.
[24] M.B. Watkins, A.S. Foster, A.L. Shluger, Journal of Physical Chemistry C 111 (2007) 15337–15341.
[25] S. Kumar, P. Schelling, Journal of Chemical Physics (2006) 125.
[26] V. Shapovalov, H. Metiu, Journal of Catalysis 245 (2007) 205–214.
[27] Z. Yang, Z. Fu, Y. Wei, Z. Lu, The Journal of Physical Chemistry C 112 (2008) 15341–15347.
[28] Z. Yang, G. Luo, Z. Lu, K. Hermansson, The Journal of Chemical Physics 127 (2007) 074704–074705.
[29] Z. Yang, G. Luo, Z. Lu, T.K. Woo, K. Hermansson, Journal of Physics: Condensed Matter 20 (2008) 035210.
[30] G. Kresse, J. Furthmuller, Computational Materials Science 6 (1996) 15–50.
[31] G. Kresse, J. Furthmuller, Physical Review B 54 (1996) 11169–11186.
[32] G. Kresse, J. Hafner, Physical Review B 47 (1993) 558–561.
[33] G. Kresse, D. Joubert, Physical Review B 59 (1999) 1758 LP–1775.
[34] J.P. Perdew, J.A. Chevary, S.H. Vosko, K.A. Jackson, M.R. Pederson, D.J. Singh, C. Fiolhais, Physical Review B 46 (1992) 6671.
[35] S. Fabris, S.d. Gironcoli, S. Baroni, G. Vicario, G. Balducci, Physical Review B 71 (2005) 041102.
[36] S. Fabris, S.d. Gironcoli, S. Baroni, G. Vicario, G. Balducci, Physical Review B 72 (2005) 237102.
[37] G. Kresse, P. Blaha, J.L.F.D. Silva, M.V. Ganduglia-Pirovano, Physical Review B 72 (2005) 237101.
[38] A.D. Mayernick, M.J. Janik, The Journal of Physical Chemistry C 112 (2008) 14955–14964.
[39] M. Nolan, S. Grigoleit, D.C. Sayle, S.C. Parker, G.W. Watson, Surface Science 576 (2005) 217–229.
[40] M. Nolan, S.C. Parker, G.W. Watson, Surface Science 595 (2005) 223–232.
[41] B. Herschend, M. Baudin, K. Hermansson, Surface Science 599 (2005) 173–186.
[42] Z. Yang, Z. Lu, G. Luo, K. Hermansson, Physics Letters A 369 (2007) 132–139.
[43] J. Waser, H.A. Levy, S.W. Peterson, Acta Crystallographica 6 (1953) 661–663.
[44] I. Lazarev, Russian Journal of Inorganic Chemistry 23 (1978) 488.
[45] J. Rogal, K. Reuter, M. Scheffler, Physical Review B (2004) 69.
[46] G. Henkelman, H. Jonsson, Journal of Chemical Physics 113 (2000) 9978–9985.
[47] G. Henkelman, B.P. Uberuaga, H. Jonsson, Journal of Chemical Physics 113 (2000) 9901–9904.
[48] G. Mills, H. Jonsson, G.K. Schenter, Surface Science 324 (1995) 305–337.
[49] C. Bozo, N. Guilhaume, E. Garbowski, M. Primet, Catalysis Today 59 (2000) 33–45.
[50] C. Bozo, N. Guilhaume, J. Herrmann, Journal of Catalysis 203 (2001) 393–406.
[51] M. Huang, S. Fabris, Journal of Physical Chemistry C 112 (2008) 8643–8648.
[52] M. Nolan, S.C. Parker, G.W. Watson, Surface Science 600 (2006) 175–178.
[53] G. Jacobs, P.M. Patterson, L. Williams, E. Chenu, D. Sparks, G. Thomas, B.H. Davis, Applied Catalysis A: General 262 (2004) 177–187.
[54] G. Jacobs, S. Ricote, U.M. Graham, P.M. Patterson, B.H. Davis, Catalysis Today 106 (2005) 259–264.
[55] J. Weaver, C. Hakanoglu, A. Antony, J. Hawkins, A. Asthagiri, Catalysis Today, in press, doi:10.1016/j.cattod.2010.06.012.
[56] Z.-P. Liu, P. Hu, Journal of the American Chemical Society 125 (2003) 1958–1967.
[57] J.R. Murdoch, Journal of Chemical Education 58 (1981) 32.
[58] S. An, C. Lu, W.L. Worrell, R.J. Gorte, J.M. Vohs, Solid State Ionics 175 (2004) 135–138.
[59] S. McIntosh, R.J. Gorte, Chemical Reviews 104 (2004) 4845–4865.
[60] E.S. Putna, J. Stubenrauch, J.M. Vohs, R.J. Gorte, Langmuir 11 (1995) 4832–4837.